

Thermally activated flux flow and inter-granular coupling properties in (Bi, Pb)-2223 superconductor added with ZnO nanoparticles

Ali Aftabi (✉ a.aftabi62@gmail.com)

University of Kurdistan, Sanandaj, Iran

Morteza Mozaffari

University of Isfahan, Isfahan, Iran

Research Article

Keywords: High-Temperature Superconductors, Vortex dynamics, Activation energy, Vortex glass, Flux pinning, Critical current density

Posted Date: March 7th, 2022

DOI: <https://doi.org/10.21203/rs.3.rs-1419443/v1>

License:   This work is licensed under a Creative Commons Attribution 4.0 International License.

[Read Full License](#)

Abstract

In high-temperature ceramic superconductors, vortices motion is caused by the strong thermal fluctuations due to the thermally activated flux flow (TAFF). The TAFF impedes the transport properties and critical current density of superconductors. It has been reported that the addition of nanoscale impurities can create artificial pinning centers that may improve flux pinning capability and inter-granular coupling in ceramic superconductors. Here, the effects of different amounts (0.0 to 1.0 wt%) of ZnO nanoparticles on the TAFF behavior and zero temperature activation energy of the $\text{Bi}_{1.6}\text{Pb}_{0.4}\text{Sr}_2\text{Ca}_2\text{Cu}_3\text{O}_{10+\delta}$ superconducting phase have been studied using the modified TAFF model. Moreover, the impacts of the additive on the inter-granular traits and the Josephson coupling energy of the superconducting phase have been investigated using AC susceptibility measurements. Results indicate that the vortex phases for all composites are divided into three vortex regions, but the temperature ranges in each region are different for various amounts of the additives. A vortex glass to vortex liquid transition at T_g was obtained from the analysis. The vortex liquid region is divided into the critical and TAFF ones. It was found that the TAFF region is shifted to the higher temperatures and gets narrower by adding the ZnO nanoparticles up to 0.2 wt%. The T_g increases from 93.8 K for the ZnO free sample to 101.0 K for the sample with 0.2 wt% ZnO nanoparticles. In addition, the zero temperature activation energy (U_0/K_B) increases from $\sim 0.4 \times 10^5$ K for the ZnO free sample to $\sim 1.4 \times 10^5$ K for the sample with 0.2 wt% ZnO nanoparticles and then decreases for higher values of additive. Moreover, it was found that the Josephson coupling energy E_j increases from ~ 0.037 eV for ZnO free sample to ~ 0.130 eV for the sample with 0.2 wt% additives. These results point out the significant improvement of the flux pinning capability and inter-granular coupling of the $\text{Bi}_{1.6}\text{Pb}_{0.4}\text{Sr}_2\text{Ca}_2\text{Cu}_3\text{O}_{10+\delta}$ superconducting phase with the addition of the 0.2 wt% ZnO nanoparticles.

1. Introduction

High-temperature ceramic superconductors opened a way for diverse applications due to the opportunity of replacing liquid helium with liquid nitrogen as a coolant which leads to overcoming the technical complexity of the cryogenic system correlated with the production of liquid helium and its high price. However, in addition to superconducting transition temperature, T_C , other essential parameters should be taken into consideration [1]. Among different ceramic superconductors, the $\text{Bi}_{1.6}\text{Pb}_{0.4}\text{Sr}_2\text{Ca}_2\text{Cu}_3\text{O}_{10+\delta}$ ((Bi, Pb)-2223) phase has a particular place owing to its remarkably high T_C (~ 110 K) and especially an excellent mechanical performance [2]. These properties make it a promising superconducting material to synthesize different kinds of samples such as wires, thin films, tapes, single crystals, and bulks for large-scale and high-current applications [3–7]. However, the performance of ceramic superconducting compounds is badly affected by inter-grains voids and inhomogeneous micro-defects, present in their bulk form [8]. In polycrystalline bulk samples, the inter-granular superconducting transport properties have become limited by the weak links caused by the grain boundaries, and the intra-granular critical current is impeded principally by the thermally activated flux flow at high temperatures and in applied magnetic fields [8]. The second critical issue is the vortex motions in the applied magnetic field, which

can easily damage the superconductivity [8]. Therefore, it can be said, the significant limitations of the (Bi, Pb)-2223 superconductor applications are the inter-grain weak links and weak flux pinning capability, which lead to weak critical current density in bulk samples.

Under equilibrium conditions, magnetic flux penetrates into the bulk of type-II superconductors above the lower critical field H_{C1} . In the mixed state ($H_{C1} < H < H_{C2}$), magnetic flux exists in the form of a hexagonal lattice of quantized vortex lines [9]. The vortices strongly interact with each other forming highly correlated configurations such as the vortex lattice [10]. Each vortex is a tube of the radius of the London magnetic penetration depth $\lambda(T)$, in which screening currents circulate around a small non-superconducting core of the radius of the coherence length $\xi(T)$. Bulk superconductivity is destroyed when the regular cores overlap at the upper critical field H_{C2} [11]. Besides, a Lorentz force $F_L = J \times B$ acts on the quantized vortices when a current J is injected into a superconductor. The critical current density $J_C(T; H)$ is then defined by the balance of the flux pinning and Lorentz forces $J_C(T; H)H = F_p(T; H)$, where F_p is the volume pinning force produced by pinning defects in the strongly interacting array of flux lines [9, 12]. Growth of the structure of the vortex lattice in weakly pinned high-temperature ceramic superconductors is of paramount importance since it determines superconducting properties that are directly suitable for applications [10, 11].

A key element to take into consideration in the study of vortex motion in ceramic superconductors is the thermal fluctuations that assist the flux motion of vortices [13]. In the mixed state, thermal fluctuations directly affect the vortex motion by the thermally activated flux flow (TAFF) and lead to the tail at the resistive transition [14]. The magnitude of thermal fluctuations can be quantified by the Ginzburg number $G_i = 10^{-9} \left(\kappa^4 T_C \gamma^2 / H_{C2}(0) \right)^2$, where $\kappa = \lambda / \xi$ is the Ginzburg-Landau parameter (λ is the London penetration depth and ξ is the superconducting coherence length) and $\gamma = \xi_{ab} / \xi_c$ represents the anisotropy ratio [14, 15]. The Ginzburg number is $G_i \sim 10^{-8} - 10^{-5}$ for conventional superconductors, while $G_i \sim 10^{-2} - 10^{-1}$ for high-temperature ceramic superconductors, which means that thermal fluctuations in ceramics are very strong [15, 16]. Strong thermal fluctuations give a rich variety of vortex phases and vortex dynamics in ceramic superconductors [15]. The vortex liquid (VL) and vortex glass (VG) phases indicate the resistive and pure superconducting states, respectively [17].

Much of the complexity of the vortex dynamics arises from the competing roles of thermal fluctuations, random pinning, and interactions between the vortices [18]. In a very clean system, it is argued that the first-order transition from a vortex liquid to an Abrikosov vortex lattice occurs at melting temperature, T_m [18–21]. When the disorders are introduced, the vortex lattice transforms into a glassy vortex state, and the vortex liquid to glass transition becomes second-order [18, 22–24]. Depending on the type and strength of the disorder, different types of vortex glass state can be obtained below the glass transition temperature, T_g [18, 22, 25]. Furthermore, in a system with intermediate disorders, the existence of an additional vortex slush phase between T_m and T_g characterized by a short-range vortex lattice correlation without a long-range correlation is proposed by Worthington et al. [26]. This vortex slush phase transition

can be regarded as the remnant of the clean system's first-order vortex lattice melting, frustrated by disorder [18, 26].

It had been shown that introducing artificial pinning centers in the superconducting matrices, apart from those which occur naturally, is a very effective method to avoid vortex motion and improve the flux pinning capability and superconducting transport properties [8, 10, 27–31]. Different techniques such as chemical doping [17, 32–34], high energy ions irradiation [31, 35], and different types of additives [1, 2, 36–43] were used in the literature for this purpose. It has been proved that the appropriate amount of nanosized additives could improve the microstructure, intergranular coupling, and flux pinning capability of the high-temperature ceramic superconductors [2, 36–39, 42, 44, 45]. Since the size of additives is smaller than the penetration depth (λ) and larger than the coherence length (ξ), they lead to intense interactions among flux lines networks and nanosized additives and consequently improve the flux pinning capability [38].

Recently, numerous reports have been published on the effects of the different nanosized additives on the superconducting properties of the (Bi, Pb)-2223 superconducting phase [2, 46–54]. The impacts of ZnO nanoparticles (NPs) on the fluctuation induced conductivity and pseudogap properties of the (Bi, Pb)-2223 phase was investigated in our previous study [11]. In the current study, the effects of the ZnO NPs on the thermally activated flux flow (TAFF) behavior and zero-temperature activation energy of the (Bi, Pb)-2223 phase are studied using the conventional Arrhenius relation and modified TAFF model. Moreover, the impacts of the ZnO NPs on inter-granular traits and Josephson coupling energy of the (Bi, Pb)-2223 phase are studied using AC susceptibility measurements.

2. Materials And Methods

Superconducting composite products of type (Bi, Pb)-2223 / (ZnO NPs) $_x$ with $0.0 \leq x \leq 1$ wt% were synthesized via the conventional solid-state reaction method using high purity Bi_2O_3 , Pb_3O_4 , SrCO_3 , CaCO_3 , and CuO powders (all of the analytical grades with minimum purities of 99.9%), as raw materials. As described in the previous study [11], the initial materials were mixed, according to the stoichiometric ratios, and grounded in an agate mortar. The ground mixture was calcined at 820°C for 24 h in the air. Then calcinated mixture reground into a fine powder. The calcining and grinding procedures were repeated three times. The resulting (Bi, Pb)-2223 precursor was added by various amounts ($x = 0.0, 0.1, 0.2, 0.3, 0.5,$ and 1.0 wt%) of ZnO NPs, with a mean crystallite size of 15 ± 2 nm. The mixed powder samples were ground in agate vials for 2 h using a planetary ball mill (FRITCH P7). The obtained mixtures were pressed into blocks ($15 \text{ mm} \times 4 \text{ mm}$ and about 2 mm in height), under the pressure of 7 tons/cm² and then subjected to heat treatment at 810°C for 120 h in the air to form the desired (Bi, Pb)-2223 / (ZnO NPs) $_x$ composites. Temperature dependence of the electrical resistivity was measured, in a magnetic field of 100 mT, by the conventional four-point probe technique. The temperature-dependent of the real part of AC susceptibility was measured using an LCR meter (FLUKE PM 6306 model).

3. Results And Discussion

3.1. Electrical resistivity analyses.

Temperature dependence of electrical resistivity in the range of 140 K down to 85 K, for (Bi, Pb)-2223 / (ZnO NPs)_x (x = 0.0, 0.1, 0.2, 0.3, 0.5 and 1 wt%) composites are plotted in Fig. 1(a). All the composites have shown metallic-like behavior in the normal state above onset critical temperature T_C^{on} , where an abrupt fall in resistivity begins, followed by a transition to zero resistance $\rho = 0$, (superconducting state) at offset temperature T_{CO} . As observed, the magnitude of the electrical resistivity in the normal state decreases with the increase of the ZnO NPs concentration up to 0.2 wt% and then increases for samples with higher ZnO NPs concentrations. The normal state electrical resistivity depends on porosity, inter-granular coupling, grain boundaries scattering, and impurities. As mentioned, the normal state resistivity is minimum for 0.2 wt% ZnO NPs added sample. It can be concluded that the porosity, heterogeneities, induced defects, and scattering produced by the grain boundaries and ZnO additive are the lowest in this sample.

The onset critical temperature T_C^{on} for different composites was determined from the crossing point of the extrapolated linear fit of the highest slope near the midpoint of the electrical resistivity jump and the linearly extrapolated straight line in the normal state of the $\rho(T)$ curve (Fig. 1(a)). The obtained values of the T_C^{on} , and T_{CO} and the broadening transition width $\Delta T_c = T_C^{on} - T_{CO}$ are summarized in Table 1. As can be observed, the T_C^{on} is about 108.5 ± 0.5 K and is almost constant for different composites. It indicates that the host crystal structure and the stoichiometry of the $\text{Bi}_{1.6}\text{Pb}_{0.4}\text{Sr}_2\text{Ca}_2\text{Cu}_3\text{O}_{10+\delta}$ superconductor phase are not affected by adding the ZnO NPs. This result agrees with the XRD results in our previous work [11], which demonstrate no change in XRD peak positions by ZnO NPs addition. It has been found that the addition of a small amount of ZnO NPs leads to the enhancement of T_{CO} from 96.0 K for ZnO free sample to 101.0 K for the sample with 0.2 Wt% ZnO NPs. For higher additive values, T_{CO} is decreased and reach 88.5 K for the sample with x = 1.0 wt%. The obtained results also show that the transition width is decreased from 12.5 K to 6.0 K as the ZnO NPs concentration enhances from 0.0 wt% to 0.2 wt%, and then increased for further enhancement of the ZnO NPs concentration until reached to 20.5 K for the sample with 1.0 wt% additive.

As observed, the $\rho(T)$ curves show two drops as the temperature is decreased below the onset of superconducting transition. To more exact studying of the transition region, we differentiated each electrical resistivity by temperature, $d\rho(T) / dT$, and plotted them as a function of temperature in Fig. 1(b). The temperature derivative of $\rho(T)$ indicates two peaks. This dual step transition is due to the granular structure and weak link nature of the samples. The first peak at T_C^{mf} (intra-granular transition temperature) is associated with intra-granular fluctuation and presents the pairing transition temperature within grains, and the second one at T_{CJ} (inter-granular transition temperature) corresponds to the inter-granular coupling. In the temperature range between T_C^{mf} and T_{CJ} , the superconducting grains are

decoupled, and the system as a whole is resistive. Below T_{CJ} the grains are coupled, or in other terms, phase-locked with zero phase difference across the inter-granular junctions [55]. The intra-granular transition temperature T_C^{mf} is determined to be sensitively unchanged by the addition of ZnO NPs and is ~ 104 K for all samples. However, the inter-granular transition temperature T_{CJ} is affected by the amount of ZnO NPs addition. As shown in Table 1, the T_{CJ} increases from 99.5 K for the ZnO free sample to its maximum value of about 102.5 K for the sample with 0.2 wt% additive and then drops for higher values of ZnO NPs and reaches 96.5 K for $x = 1.0$ wt%. These results show that the inter-granular coupling between grains improves by increasing the ZnO NPs concentration up to 0.2 wt%.

Table 1
The deduced parameters from temperature dependance of electrical resistivity measurements.

x (wt%)	T_C^{on} (K)	T_{CO} (K)	ΔT_C (K)	T_C^{mf} (K)	T_{CJ} (K)	hole concentration, p
0	108.5	96.0	12.5	104.0	99.5	0.121
0.1	109.0	100.0	9.0	104.0	102.0	0.127
0.2	108.0	101.5	6.5	104.0	102.5	0.129
0.3	108.5	96.0	12.5	104.0	98.5	0.121
0.5	108.5	94.0	14.5	104.0	97.5	0.118
1	109.0	88.5	20.5	104.0	96.5	0.111

Furthermore, it is well-known that the variation of the hole concentration in the CuO_2 planes could affect the T_{CO} . The concentration of hole carrier per copper ion, p , can be determined using the following expression [56, 57]:

$$p = 0.16 - \left[\left(1 - \frac{T_{CO}}{T_C^{max}} \right) / 82.6 \right]^{0.5}$$

1

where T_C^{max} is the highest critical temperature of (Bi, Pb)-2223 superconducting phase and taken as 110 K. The calculated values for hole concentration are recorded in Table 1. With increasing the content of ZnO NPs from 0.0 to 0.2 wt%, the hole concentration, p , increases from 0.121 to 0.129. For higher amounts of ZnO NPs, it decreases and reaches 0.111 for $x = 1.0$ wt%. The improved inter-grain connectivity and grain morphology are the primary sources of increased hole carrier concentration after the inclusion of ZnO NPs in the (Bi, Pb)-2223 matrix.

3.2. Thermally activated flux flow analyses.

In the mixed state of high-temperature superconductors, disorders and defects induce barriers for the vortex motion, and three different situations can be expected; (1) unpinned vortex liquid (UVL) state: the energy barrier U_0 is lower than the temperature and can be neglected, (2) Thermally activated flux flow (TAFF) regime: The energy barrier U_0 is higher than the temperature and plays a vital role in vortex motion. (3) Vortex-glass (VG) state: the barrier grows unlimitedly at low critical current density and the linear resistivity drops to zero [58]. In the TAFF and UVL regimes, the temperature dependence of resistivity is defined according to the TAFF theory as [59, 60]:

$$\rho(T, B) = \left(2\nu_0LB/J\right) \exp\left(-J_{C0}BVL/T\right) \sinh(JBVL/T)$$

2

where ν_0 is an attempt frequency for a flux bundle hopping, L is the hopping distance, B is the magnetic induction, J is the applied current density, J_{C0} is the critical current density in the absence of flux creep, V is the bundle volume, and T is the temperature [61]. If the applied current is small enough so that $JBVL/T \ll 1$, Eq. (2) can be simplified to

$$\rho(T, B) = \left(2\rho_c U/T\right) \exp(-U/T) = \rho_{0f} \exp(-U/T)$$

3

where $U = J_{C0}BVL$ is the thermal activation energy and $\rho_c = \nu_0LB/J_{C0}$. The detailed definitions of U and ρ_c indicate that $2\rho_c U/T$ is dependent on temperature and magnetic field [31]. In cuprates and FeAs-based superconductors, $\rho_{0f} = 2\rho_c U/T$ is assumed as a temperature-independent constant [14, 31, 58, 61]. The temperature dependence of the activation energy U is usually assumed as $U(T, B) = U_0(B)(1 - T/T_C)$, where U_0 is the apparent activation energy. In this assumption, the natural logarithm of electrical resistivity is expressed as

$$\ln\rho(T, B) = \ln\rho_0 - U_0(B)/T$$

4

where $\ln\rho_0 = \ln\rho_{0f} + U_0(B)/T_C$. This equation is known as the Arrhenius relation [31, 61, 62]. According to the Arrhenius relation, the plot of $\ln\rho$ vs. $1/T$ should show a linear behavior in the TAFF region. Consequently, the temperature dependence of the derivative $D = -\partial(\ln\rho)/\partial(T^{-1})$ shows a

distinct plateau in the TAFF region. The plots of $-\partial(\ln\rho)/\partial(T^{-1})$ vs. T , for composites with $x=0.0, 0.2$, and 1.0 wt%, as typical samples, are depicted in Figs. 2(a-c) to indicate the temperature region that satisfies the Arrhenius relationship. As can be observed, however, the plateau is not seen but rather increases as temperature decreases. Such behavior has been observed in cuprates and iron-based superconductors [14, 17, 31, 61]. To solve this contradiction in the TAFF model, Zhang et al. [63, 64] established a new model, called the modified TAFF model, by suggesting non-linear activated energy of the form $U(T, B) = U_0(B)(1 - T/T_C)^q$. By applying this non-linear activation energy, in the TAFF regime, to Eq. (3), it can be derived that

$$\ln\rho = \ln(2\rho_c U_0) + q\ln(1 - T/T_C) - \ln T - U_0(1 - T/T_C)^q/T$$

5

,

and

$$-\partial\ln\rho/\partial T^{-1} = [U_0(1 - T/T_C)^q - T][1 + qT/(T_C - T)]$$

6

,

where q is a free parameter. According to the condensation model, $q=2$ is expected in the case of high-temperature superconductors with large anisotropy, which shows 2D vortex behavior, whereas $q=1.5$ was seen in high-temperature superconductors with small anisotropy showing 3D vortex behavior [14, 15, 58]. To determine the TAFF regime, zero temperature activation energy U_0 , and q parameter, the $-\partial\ln\rho/\partial T^{-1}$ vs. T , $\ln\rho$ vs. T , and $\ln\rho$ vs. $1/T$ plots were fitted using Eqs. (5 and 6). The $\ln\rho$ vs. T curves for composites with $x = 0.0, 0.2$ and 1.0 wt% are shown in Figs. 2(d-f), as typical samples. The red solid line shows the best fit with Eqs. (5). Moreover, the $\ln\rho$ vs. $1/T$ curves for different samples are represented in Fig. 3. The solid lines demonstrate the best fits with the modified TAFF model. As can be observed, these best fits agree well with the experimental values in the temperature range $T^* < T < T_k$, which indicate the TAFF regions for different samples. The T_k is defined as the temperature on the higher side deviating from the TAFF fitting. It is the characteristic temperature that determines the transition temperature from the TAFF regime to the unpinned vortex liquid phase [58]. The T^* is defined as the critical temperature below which the curve deviates from TAFF fitting. It represents the upper-temperature limit of the critical region for the vortex liquid to vortex glass state transition [65].

The obtained values for T_k , T^* and temperature width of TAFF region, $\Delta T_{TAFF} = T_k - T^*$, are summarized in Table 2. As can be observed, the T_k and T^* increase with the increase of the ZnO NPs concentration up to 0.2 wt% and then decrease for higher values of the additive. The ΔT_{TAFF} is decreased from 6 K for the ZnO-free sample to 4 K for the sample with $x = 0.2$ wt% and then increased for

higher values of the ZnO NPs and reached 12 K for the sample with $x = 1.0$ wt%. These results indicate that the TAFF region is shifted to the higher temperatures and gets narrower by adding the ZnO NPs up to 0.2%. For higher values of additive, the TAFF region gets wider and transferred to lower temperatures. The deduced values for zero temperature activation energy U_0 , determined by the fitting of the experimental data, using Eqs. (5 and 6) in the TAFF region, are shown in Fig. 4. As seen, by increasing the ZnO NPs concentration, U_0 increases from $\sim 0.4 \times 10^5$ K for the ZnO free sample to $\sim 1.4 \times 10^5$ K in the sample with 0.2 wt% ZnO NPs and then decreases for higher values of additive and reaches $\sim 0.17 \times 10^5$ K for the sample with 1.0 wt% ZnO. This indicates that the addition of the 0.2 wt% ZnO NPs improves flux pinning capability of the (Bi, Pb)-2223 superconducting phase significantly.

Table 2
The deduced parameters from TAFF analyses.

x (wt%)	T* (K)	T ^K (K)	ΔT_{TAFF} (K)	T _g (K)	s	U ₀
0	97.0	103.0	6.0	93.8	2.4	40894
0.1	101.0	105.0	4.0	99.8	1.5	83416
0.2	103.0	105.5	2.5	101.0	2.3	146217
0.3	98.0	103.0	5.0	94.9	1.9	34247
0.5	96.5	102.0	5.5	92.9	2.4	28935
1.0	89.5	101.5	12.0	87.4	2.0	17082

As observed in Figs. 2(d-f), the $\ln\rho$ curves begin to deviate upward from the solid red line, interpreted as the TAFF regime, in the temperature region below T^* . It indicates a second-order phase transition from the vortex liquid phase to the vortex glass phase [14]. From this point of view, the deviation below T^* is due to the increased effective activation energy caused by gradual vortex glass development as the temperature decreases in the vortex liquid phase. This temperature region is called a critical region present in the vortex liquid phase [14]. In the critical region, the vortex glass theory [66] predicts the temperature dependence of the linear resistivity through the relation $\rho(T) \propto (T - T_g)^s$, where $s = \nu(z + 2 - d)$ is the critical exponent and d is the dimensionality of the sample ($d=3$ in the present samples), ν is the static index for vortex-glass correlation length, and z is the dynamic index for correlation time. According to Liu et al. [67], the electrical resistivity is given as

$$\rho(T) = \rho_n \left[\exp(-U_{\text{eff}}/k_B T) \right]^s$$

7

and the thermal activity energy in the critical region, present in the vortex liquid phase, is given as [14]

$$U_{eff} = k_B T \frac{(T_C - T)}{(T_C - T_g)}$$

8

Moreover, according to the vortex glass phase transition theory [18, 23, 60], at the glass temperature T_g , one has $\rho(T_g) = 0$. At the critical temperature T_C , one has $\rho(T_C) = \rho_n$, thus $(U_{eff}/k_B T) = 0$. Hence one has $0 \leq U_{eff}/k_B T \leq 1$ in the temperature region $T_g \leq T \leq T_C$. A first-order series expansion in Eq. (7) around T_C gives $\rho(T) = \rho_n \left[1 - (U_{eff}/k_B T) \right]^s$. Using Eq. (8) the temperature-dependent resistance in the vortex glass critical region is obtained as

$$\rho = \rho_n \left(\frac{T - T_g}{T_C - T_g} \right)^s$$

9

which is consistent with the vortex-glass theory. The experimental data in the vortex glass critical region has been fitted with Eq. (9). The dash lines in Figs. (2 and 3) represent the corresponding best fits for different composites. As can be seen, the fits agree well with the experimental values below T^* . From the fitting using Eq. (9), the vortex glass temperature T_g and critical exponent s were evaluated. According to the vortex-glass theory, $s \leq 2.7$ corresponds to the 2D vortex glass state while the values of s in between 2.7 to 8.5 correspond to the 3D vortex glass state [14, 17, 58]. As represented in Table 2, the obtained s values for different composites are smaller than 2.7, which indicates the 2D vortex glass state for the prepared composites. Therefore, all the samples undergo a phase transition from 2D vortex glass with $s < 2.7$ to 2D vortex liquid with $q = 2$ at T_g , which means that the 2D correlation created below T_g is maintained up to high temperature [14]. In other words, the 2D vortices in vortex liquid, which are determined from the q -values discussed above, are frozen into the 2D vortex glass with decreasing temperature, in agreement with the vortex glass theory [58]. As recorded in Table 2, by increasing the ZnO NPs concentration, the vortex glass transition temperature T_g increases from 93.8 K for the ZnO free sample to 101.0 K for the sample with 0.2 wt% ZnO NPs and then drops for more additives until it reaches 87.4 K for the sample with 1.0 wt% ZnO NPs.

To verify the accuracy of the obtained values for U_0 from the above indirect approach, the temperature dependence of activation energy was calculated directly from the measurement data using the Arrhenius equation (Eq. (3)) by $U(T, H) = - T \ln \left[\rho(T, H) / \rho_{0f} \right]$. The calculated temperature dependence of activation energy for different composites has been shown in Figs. 5(a-f). As observed, all the samples show a similar temperature dependence. As the temperature decreases from the high temperatures the

magnitude of $U(T, H)$ increases slowly, then increases steeply. The TAFF region for different composites is also highlighted in Figs. 5(a-f), which has a different temperature range depending on the amount of ZnO NPs additive. As mentioned above, the temperature dependence of the activation energy on the TAFF region is given by $U(T, H) = U_0(H)(1 - T/T_C)^q$. The $U(T, H)$ had been calculated, using obtained values for U_0 , T_C and q , and has been plotted by solid red lines for different composites in Figs. 5(a-f). As observed in the figures, the agreement between the experimental data and the $U(T, H) = U_0(H)(1 - T/T_C)^q$ relation, in the TAFF region, is excellent in all composites.

3.3. AC susceptibility analyses.

The AC susceptibility measurement is extensively employed as a non-destructive and effective tool for understanding and characterization of the intra-grain and inter-grain components in the polycrystalline high-temperature superconductors [40, 45, 55, 68–70]. The plots of the real part of AC susceptibility, χ' , and its derivative, $d\chi'/dT$, versus temperature at a frequency of 300 Hz and the AC background magnetic field of 250 A/m, for different composite samples are displayed in Figs. 6(a) and (b), respectively. A characteristic feature of the AC susceptibility in HTSCs is the presence of double drops in χ' (T) and correspondingly two peaks in $d\chi'/dT$. The first peak at T_C is related to the transition to superconducting state within grains and correlated to the intra-granular properties, and the second peak at T_{CJ} is related to coupling matrix and correlated to the inter-granular properties. As mentioned above, in the temperature range $T_{CJ} < T < T_C$, the superconducting grains are decoupled, and the system as a whole is resistive. Below T_{CJ} , the grains are coupled, or in other terms, phase-locked with zero phase difference across the inter-granular junctions. Wide/narrow separation of intra- and inter-granular peaks signifies a worse/better connection among the grains. As demonstrated in Fig. 6(b), T_C is sensitively unchanged with ZnO NPs addition. However, T_{CJ} associated with the occurrence of the weak links network among grains is sensitive to the amount of ZnO additive. This result indicates that the addition of the ZnO NPs does not have a sensitive effect on the intra-granular properties of samples, while it affects the inter-granular properties. T_{CJ} was determined from the derivative of χ' versus temperature graph (Fig. 6(b)). As shown in Fig. 6(c), by increasing the ZnO NPs concentration, T_{CJ} increases from 95.5 K for the ZnO-free sample to 102 K for the sample with $x = 0.2$ wt% and then shows a decreasing behavior for higher values of ZnO NPs until it reaches to 93 K for the sample with $x = 1$ wt%. These results can be a clear sign of enhanced inter-granular properties with ZnO NPs addition. The observed behavior has a good agreement with obtained values from resistivity measurements.

High-temperature superconductor materials can be modeled as an array of weakly Josephson coupling. Grains coupling takes place via the Josephson currents in the layers among grains [40]. The Josephson coupling energy can be expressed as [40]:

$$E_j = \frac{h}{4\pi e} I_0$$

where h is the Planck constant, e is the elementary charge, and I_0 is the maximum Josephson's current that passes across the grain boundaries and according to Ambegaokar Baratoff expressed as [40, 71]:

$$I_0 = 1.57 \times 10^{-8} \times \frac{T_C}{(T_C - T_{CJ})} \times 100$$

11

The Josephson coupling energy, E_j , for different composites, has been calculated using the above equations, and its value, at $H= 250$ A/m, as a function of the ZnO NPs concentration is plotted in Fig. 6(c). As seen, the E_j is increased from ~ 0.037 eV to ~ 0.130 eV by increasing the ZnO NPs concentration from 0.0 to 0.2 wt% and then is decreased for higher ZnO NPs concentrations until it reaches 0.029 eV for the sample with 1.0 wt% additive. This result points out the significant improvement of the inter-granular coupling with the addition of the 0.2 wt% ZnO NPs. The stronger inter-granular Josephson coupling energy leads to the stronger trapping force, and, therefore, the greater critical current density will be.

3.4. V-I analyses.

To investigate the effects of the ZnO NPs addition on the critical current density, the V-I curve for different samples has been recorded at 77 K by the four-point-probe technique. The obtained V-J curves are plotted in Fig. 7. Critical current densities were determined from the V-J curves, using the criterion of $2 \mu\text{V}/\text{cm}$. As observed, the critical current density increases from ~ 114 A/cm² for ZnO free sample to ~ 249 A/cm² for the sample with 0.2 wt% additives. For higher values of ZnO NPs, it decreases and reaches ~ 45 A/cm² for the sample with 1.0 wt% additive. The improvement of the critical current density by adding the ZnO NPs up to 0.2 wt% is attributed to enhancing the inter-granular Josephson coupling energy and activation energy.

4. Conclusion

In conclusion, the impacts of adding different amounts (0.0 to 1.0 wt%) of ZnO nanoparticles (NPs), with a mean crystallite size of 15 ± 2 nm, on the thermally activated flux flow (TAFF) behavior and zero-temperature activation energy of the $\text{Bi}_{1.6}\text{Pb}_{0.4}\text{Sr}_2\text{Ca}_2\text{Cu}_3\text{O}_{10+\delta}$ superconducting phase have been investigated using the modified TAFF model. Moreover, the effects of the ZnO NPs additive on the inter-granular traits and Josephson coupling energy of the superconducting phase have been studied, using AC susceptibility measurement. The obtained results indicate that the vortex phases for all composites are divided into three vortex regions, but the temperature ranges in each region are different for various amounts of the ZnO NPs. All composites show a 2D vortex glass region below the T_g which is well understood by the vortex glass theory. Vortex liquid region exists above T_g that is well described by

modified TAFF model but is divided into critical and TAFF regions due to the difference in the temperature dependency of the activation energy. For all composites, in the critical region, the effective activation energy is well described by $U_{eff} = k_B T \left[(T_C - T) / (T_C - T_g) \right]$, and in the TAFF region is well fitted by $U(T, H) = U_0(H) (1 - T/T_C)^q$ with $q=2$ that indicates the 2D vortex liquid behavior. Through the analysis with the modified TAFF model, it was found that the TAFF region is shifted to the higher temperatures and gets narrower by the addition of the ZnO NPs up to 0.2 wt%. For more additives, the TAFF region gets wider and transferred to lower temperatures. The vortex glass to vortex liquid transition temperature, T_g , increases from 93.8 K for the ZnO free sample to 101.0 K for the sample with 0.2 wt% ZnO nanoparticles and then drops for higher values of additive until it reaches 87.4 K for the sample with 1.0 wt% ZnO NPs. In addition, by increasing the ZnO NPs concentration, the zero temperature activation energy increases from $\sim 0.4 \times 10^5$ K for the ZnO free sample to $\sim 1.4 \times 10^5$ K for the sample with 0.2 wt% ZnO NPs and then decreases for more additives. From AC susceptibility measurements, important parameters including inter-granular coupling temperature T_{CJ} and Josephson coupling energy E_j were estimated and discussed. It was found that inter-granular coupling is improved with ZnO NPs addition significantly. The E_j value increases from ~ 0.037 eV for the ZnO free sample to ~ 0.130 eV for the sample with 0.2 wt% ZnO additive. These results point out the significant improvement of the inter-granular coupling and flux pinning capability in the $\text{Bi}_{1.6}\text{Pb}_{0.4}\text{Sr}_2\text{Ca}_2\text{Cu}_3\text{O}_{10+\delta}$ superconducting phase with adding of the 0.2 wt% ZnO NPs.

Declarations

Declaration of interests

The authors declare that they have no known competing financial interests or personal relationships that could have appeared to influence the work reported in this paper.

References

1. Hannachi E, Almessiere MA, Slimani Y, Alshamrani RB, Yasin G, Ben Azzouz F. Preparation and characterization of high-Tc $(\text{YBa}_2\text{Cu}_3\text{O}_{7-\delta})_{1-x}/(\text{CNTs})_x$ superconductors with highly boosted superconducting performances. *Ceram Int* 2021;47:23539–48. <https://doi.org/https://doi.org/10.1016/j.ceramint.2021.05.071>.
2. Loudhaief N, Ben Salem M, Labiadh H, Zouaoui M. Electrical properties and fluctuation induced conductivity studies of Bi-based superconductors added by CuS nanoparticles synthesized through the aqueous route. *Mater Chem Phys* 2020;242:122464. <https://doi.org/10.1016/j.matchemphys.2019.122464>.
3. Larbalestier DC, Jiang J, Trociewitz UP, Kametani F, Scheuerlein C, Dalban-Canassy M, et al. Isotropic round-wire multifilament cuprate superconductor for generation of magnetic fields above 30 T. *Nat Mater* 2014;13:375–81. <https://doi.org/10.1038/nmat3887>.

4. Kametani F, Jiang J, Matras M, Abraimov D, Hellstrom EE, Larbalestier DC. Comparison of growth texture in round Bi2212 and flat Bi2223 wires and its relation to high critical current density development. *Sci Rep* 2015;5:8285. <https://doi.org/10.1038/srep08285>.
5. Oh JY, Le TM, Pham AT, Tran DH, Yang DS, Kang B. Role of interlayer coupling in alkaline-substituted (Bi, Pb)-2223 superconductors. *J Alloys Compd* 2019;804:348–52. <https://doi.org/10.1016/j.jallcom.2019.07.029>.
6. Zou C, Hao Z, Li H, Li X, Ye S, Yu L, et al. Effect of Structural Supermodulation on Superconductivity in Trilayer Cuprate Bi2Sr2Ca2Cu3O10. *Phys Rev Lett* 2020;124:47003. <https://doi.org/10.1103/PhysRevLett.124.047003>.
7. Chen X-J, Struzhkin V V, Yu Y, Goncharov AF, Lin C-T, Mao H, et al. Enhancement of superconductivity by pressure-driven competition in electronic order. *Nature* 2010;466:950–3. <https://doi.org/10.1038/nature09293>.
8. Hussain G, Jabbar A, Qasim I, Mumtaz M, Nadeem K, Zubair M, et al. Activation energy and excess conductivity analysis of (Ag)_x/CuTl-1223 nano-superconductor composites. *J Appl Phys* 2014;116:103911. <https://doi.org/10.1063/1.4895051>.
9. Gurevich A. Superconductivity: Critical Currents. In: Bassani F, Liedl GL, Wyder PBT-E of CMP, editors. *Encycl. Condens. Matter Phys.*, Oxford: Elsevier; 2005, p. 82–8. <https://doi.org/10.1016/B0-12-369401-9/00737-3>.
10. Arumugam S, Krishnan M, Ishigaki K, Gouchi J, Pervin R, Selvan GK, et al. Enhancement of superconducting properties and flux pinning mechanism on Cr0.0005NbSe2 single crystal under Hydrostatic pressure. *Sci Rep* 2019;9:347. <https://doi.org/10.1038/s41598-018-36672-x>.
11. Aftabi A, Mozaffari M. Fluctuation induced conductivity and pseudogap state studies of Bi1.6Pb0.4Sr2Ca2Cu3O10 + δ superconductor added with ZnO nanoparticles. *Sci Rep* 2021;11:4341. <https://doi.org/10.1038/s41598-021-83218-9>.
12. Matsumoto K, Mele P. Artificial pinning center technology to enhance vortex pinning in YBCO coated conductors. *Supercond Sci Technol* 2010;23:14001. <https://doi.org/10.1088/0953-2048/23/1/014001>.
13. Labrag A, Bghour M, Abou El Hassan A, El Hamidi H, Taoufik A, Laasri S. The activation energy U(T,B) in high temperature superconductor. *Eur Phys J Appl Phys* 2020;92:20601. <https://doi.org/10.1051/epjap/2020200223>.
14. Choi WJ, Seo YI, Ahmad D, Kwon YS. Thermally activated flux motion in optimally electron-doped (Ca_{0.85}La_{0.15})₁₀(Pt₃As₈)(Fe₂As₂)₅ and Ca₁₀(Pt₃As₈)(Fe_{0.92}Pt_{0.08})₂As₂)₅ single crystals. *Results Phys* 2020;19:103430. <https://doi.org/https://doi.org/10.1016/j.rinp.2020.103430>.
15. Jang Song Y, Kang B, Rhee J-S, Kwon YS. Thermally activated flux flow and fluctuation conductivity in LiFeAs single crystal. *EPL (Europhysics Lett)* 2012;97:47003. <https://doi.org/10.1209/0295-5075/97/47003>.
16. Mikitik GP, Brandt EH. Peak effect, vortex-lattice melting line, and order-disorder transition in conventional and high T_c superconductors. *Phys Rev B* 2001;64:184514.

- <https://doi.org/10.1103/PhysRevB.64.184514>.
17. Kumar R, Varma GD. Study of TAFF and vortex phase of $\text{FexTe}_{0.60}\text{Se}_{0.40}$ ($0.970 \leq x \leq 1.030$) single crystals. *Phys Scr* 2020;95:45814. <https://doi.org/10.1088/1402-4896/ab71bf>.
 18. Xing X, Yi X, Li M, Meng Y, Mu G, Ge J-Y, et al. Vortex phase diagram in 12442-type $\text{RbCa}_2\text{Fe}_4\text{As}_4\text{F}_2$ single crystal revealed by magneto-transport and magnetization measurements. *Supercond Sci Technol* 2020;33:114005. <https://doi.org/10.1088/1361-6668/abb35f>.
 19. Safar H, Gammel PL, Huse DA, Bishop DJ, Rice JP, Ginsberg DM. Experimental evidence for a first-order vortex-lattice-melting transition in untwinned, single crystal $\text{YBa}_2\text{Cu}_3\text{O}_7$. *Phys Rev Lett* 1992;69:824–7. <https://doi.org/10.1103/PhysRevLett.69.824>.
 20. Kwok WK, Fendrich J, Fleshler S, Welp U, Downey J, Crabtree GW. Vortex liquid disorder and the first order melting transition in $\text{YBa}_2\text{Cu}_3\text{O}_7$. *Phys Rev Lett* 1994;72:1092–5. <https://doi.org/10.1103/PhysRevLett.72.1092>.
 21. Welp U, Fendrich JA, Kwok WK, Crabtree GW, Veal BW. Thermodynamic Evidence for a Flux Line Lattice Melting Transition in $\text{YBa}_2\text{Cu}_3\text{O}_7$. *Phys Rev Lett* 1996;76:4809–12. <https://doi.org/10.1103/PhysRevLett.76.4809>.
 22. Andersson M, Rydh A, Rapp Ö. Scaling of the vortex-liquid resistivity in optimally doped and oxygen-deficient $\text{YBa}_2\text{Cu}_3\text{O}_7$ single crystals. *Phys Rev B* 2001;63:184511. <https://doi.org/10.1103/PhysRevB.63.184511>.
 23. Fisher DS, Fisher MPA, Huse DA. Thermal fluctuations, quenched disorder, phase transitions, and transport in type-II superconductors. *Phys Rev B* 1991;43:130–59. <https://doi.org/10.1103/PhysRevB.43.130>.
 24. Koch RH, Foglietti V, Gallagher WJ, Koren G, Gupta A, Fisher MPA. Experimental evidence for vortex-glass superconductivity in Y-Ba-Cu-O. *Phys Rev Lett* 1989;63:1511–4. <https://doi.org/10.1103/PhysRevLett.63.1511>.
 25. Nishizaki T, Naito T, Kobayashi N. Anomalous magnetization and field-driven disordering transition of a vortex lattice in untwinned $\text{YBa}_2\text{Cu}_3\text{O}_y$. *Phys Rev B* 1998;58:11169–72. <https://doi.org/10.1103/PhysRevB.58.11169>.
 26. Worthington TK, Fisher MPA, Huse DA, Toner J, Marwick AD, Zabel T, et al. Observation of separate vortex-melting and vortex-glass transitions in defect-enhanced $\text{YBa}_2\text{Cu}_3\text{O}_7$ single crystals. *Phys Rev B* 1992;46:11854–61. <https://doi.org/10.1103/PhysRevB.46.11854>.
 27. Giapintzakis J, Lee WC, Rice JP, Ginsberg DM, Robertson IM, Wheeler R, et al. Production and identification of flux-pinning defects by electron irradiation in $\text{YBa}_2\text{Cu}_3\text{O}_{7-x}$ single crystals. *Phys Rev B* 1992;45:10677–83. <https://doi.org/10.1103/PhysRevB.45.10677>.
 28. Khan NA, Mumtaz M. Absence of a pair-breaking mechanism in $\text{Cu}_{0.5}\text{Tl}_{0.5}\text{Ba}_2\text{Ca}_3\text{Cu}_4\text{ZnyO}_{12-\delta}$. *Phys Rev B* 2008;77:54507. <https://doi.org/10.1103/PhysRevB.77.054507>.
 29. Larbalestier D, Gurevich A, Feldmann DM, Polyanskii A. High- T_c superconducting materials for electric power applications. *Nature* 2001;414:368–77. <https://doi.org/10.1038/35104654>.

30. Hari Babu N, Reddy ES, Cardwell DA, Campbell AM, Tarrant CD, Schneider KR. Artificial flux pinning centers in large, single-grain (RE)-Ba-Cu-O superconductors. *Appl Phys Lett* 2003;83:4806–8. <https://doi.org/10.1063/1.1631738>.
31. Choi WJ, Ahmad D, Seo YI, Ko RK, Kwon YS. Effect of the proton irradiation on the thermally activated flux flow in superconducting SmBCO coated conductors. *Sci Rep* 2020;10:2017. <https://doi.org/10.1038/s41598-020-58936-1>.
32. Arif M, Rahim M, Khan NA. Enhanced coherence length and interplane coupling by Ti doping in (Cu, Tl)-1223 superconductors: Para conductivity analyses. *Ceram Int* 2020;46:3218–23. <https://doi.org/https://doi.org/10.1016/j.ceramint.2019.10.026>.
33. Hussain S, Ali J, Khan NA, Raza A. Effect of Cd intercalation on the superconducting properties of (Cu_{0.5-y}K_yTl_{0.5})Ba₂Ca₂Cu_{3-x}Cd_xO_{10-δ} (y = 0, 0.25; x = 0, 0.5, 1.0, 1.5, 2.0) superconductors. *J Alloys Compd* 2020;817:1–11. <https://doi.org/10.1016/j.jallcom.2019.152697>.
34. Harabor A, Rotaru P, Harabor NA. Effect of Ni substitute in off-stoichiometric Bi(Pb)-Sr-Ca-Cu(Ni)-O superconductor. Excess conductivity, XRD analysis and thermal behaviour. *Ceram Int* 2019;45:2742–50. <https://doi.org/10.1016/j.ceramint.2018.09.060>.
35. Litvinov Y V., Vovk R V., Dobrovolskiy O V. Evolution of excess conductivity in YBCO single crystals after irradiation with fast electrons. *Phys C Supercond Its Appl* 2020;573:1353645. <https://doi.org/10.1016/j.physc.2020.1353645>.
36. Algarni R, Almessiere MA, Slimani Y, Hannachi E, Ben Azzouz F. Enhanced critical current density and flux pinning traits with Dy₂O₃ nanoparticles added to YBa₂Cu₃O_{7-d} superconductor. *J Alloys Compd* 2021;852:157019. <https://doi.org/https://doi.org/10.1016/j.jallcom.2020.157019>.
37. Ghahramani S, Shams G, Soltani Z. Comparative Investigation of the Effect of Titanium Oxide Nanoparticles on Some Superconducting Parameters of Y₃Ba₅Cu₈O_{18 ± δ} and Y₁Ba₂Cu₃O_{7 – δ} Composites. *J Electron Mater* 2021;50:4727–40. <https://doi.org/10.1007/s11664-021-09012-5>.
38. Almessiere MA, Hannachi E, Slimani Y, Yasin G, Mumtaz M, Koblischka MR, et al. Dimensionality and superconducting parameters of YBa₂Cu₃O_{7 – d}/(WO₃ NPs)_x composites deduced from excess conductivity analysis. *Mater Chem Phys* 2020;243:122665. <https://doi.org/https://doi.org/10.1016/j.matchemphys.2020.122665>.
39. Hannachi E, Slimani Y, Al-qwairi FO, Almessiere MA, Ben Azzouz F. Comparative study of thermal fluctuation induced conductivity in YBa₂Cu₃O_{7-d} containing Nano-Zn_{0.95}Mn_{0.05}O and Nano-Al₂O₃ particles. *Solid State Sci* 2020;105:106264. <https://doi.org/https://doi.org/10.1016/j.solidstatesciences.2020.106264>.
40. Hannachi E, Almessiere MA, Slimani Y, Baykal A, Ben Azzouz F. AC susceptibility investigation of YBCO superconductor added by carbon nanotubes. *J Alloys Compd* 2020;812:152150. <https://doi.org/10.1016/j.jallcom.2019.152150>.
41. Sahoo B, Routray KL, Panda B, Samal D, Behera D. Excess conductivity and magnetization of CoFe₂O₄ combined with Y₁Ba₂Cu₃O_{7-δ} as a superconductor. *J Phys Chem Solids* 2019;132:187–96. <https://doi.org/10.1016/j.jpcs.2019.04.035>.

42. Slimani Y, Hannachi E, Ekicibil A, Almessiere MA, Ben Azzouz F. Investigation of the impact of nano-sized wires and particles TiO₂ on Y-123 superconductor performance. *J Alloys Compd* 2019;781:664–73. <https://doi.org/10.1016/j.jallcom.2018.12.062>.
43. Aftabi A, Mozaffari M, Kameli P. The effect of Al₂O₃ nanopowder addition on the phase formation and the superconducting properties of Bi_{1.6}Pb_{0.4}Sr_{1.9}Ca_{2.1}Cu₃O_{10-y}. *Iran J Phys Res* 2019;9:65–9.
44. Aftabi A, Mozaffari M. Intergranular Coupling, Critical Current Density, and Phase Formation Enhancement of Polycrystalline Bi_{1.6}Pb_{0.4}Sr₂Ca₂Cu₃O_{10-y} Superconductors by α-Al₂O₃ Nanoparticle Addition. *J Supercond Nov Magn* 2015;28:2337–43. <https://doi.org/10.1007/s10948-015-3040-7>.
45. Alotaibi SA, Slimani Y, Hannachi E, Almessiere MA, Yasin G, Al-qwairi FO, et al. Intergranular properties of polycrystalline YBa₂Cu₃O_{7-δ} superconductor added with nanoparticles of WO₃ and BaTiO₃ as artificial pinning centers. *Ceram Int* 2021;47:34260–8. <https://doi.org/10.1016/j.ceramint.2021.08.336>.
46. Habanjar K, El Haj Hassan F, Awad R. Comparative studies for the physical properties of superconducting (BaSnO₃)_x(Bi,Pb)-2223 samples determined from excess conductivity and thermoelectric power analysis. *Mater Res Express* 2019;6:096001. <https://doi.org/10.1088/2053-1591/ab2b07>.
47. Awad R, Rahal HT, Abdel-Gaber AM, Abou-Aly AI. Excess Conductivity and Magnetoconductivity Analysis of (NiO)_x (Bi,Pb)-2223 Superconducting Phase. *J Supercond Nov Magn* 2019;32:2733–7. <https://doi.org/10.1007/s10948-019-5035-2>.
48. Roumié M, Abdeen W, Awad R, Korek M, Hassan I, Mawassi R. Excess conductivity analysis of Bi_{1.8}Pb_{0.4}Sr₂Ca₂Cu₃O_{10+δ} added with Nano-ZnO and Nano-Fe₂O₃. *J Low Temp Phys* 2014;174:45–63. <https://doi.org/10.1007/s10909-013-0945-z>.
49. Fallah-Arani H, Baghshahi S, Sedghi A, Riahi-Noori N. Enhancement in the performance of BSCCO (Bi-2223) superconductor with functionalized TiO₂ nanorod additive. *Ceram Int* 2019;45:21878–86. <https://doi.org/10.1016/j.ceramint.2019.07.198>.
50. Yahya NAA, Abd-Shukor R. Effect of nano-sized PbO on the transport critical current density of (Bi_{1.6}Pb_{0.4}Sr₂Ca₂Cu₃O₁₀)/Ag tapes. *Ceram Int* 2014;40:5197–200. <https://doi.org/http://dx.doi.org/10.1016/j.ceramint.2013.10.078>.
51. Saouadel A, Saouadel A, Boudjadja Y, Bouchehou H, Allag H, Altintas SP. Effects of thallium fluoride and yttrium on structure, electrical properties and ac losses susceptibility of (Bi,Pb)-2234 superconductors. *Cryogenics (Guildf)* 2021;117:103326. <https://doi.org/https://doi.org/10.1016/j.cryogenics.2021.103326>.
52. Pham AT, Tran DT, Pham HH, Nam NH, Tai LT, Tran DH. Improvement of flux pinning properties in Fe₃O₄ nanoparticle-doped Bi_{1.6}Pb_{0.4}Sr₂Ca₂Cu₃O_{10+δ} superconductors. *Mater Lett* 2021;298:130015. <https://doi.org/https://doi.org/10.1016/j.matlet.2021.130015>.
53. Shalaby MS, Hamed MH, Yousif NM, Hashem HM. The impact of the addition of Bi₂Te₃ nanoparticles on the structural and the magnetic properties of the Bi-2223 high-T_c superconductor.

- Ceram Int 2021;47:25236–48. <https://doi.org/https://doi.org/10.1016/j.ceramint.2021.05.244>.
54. Fallah-Arani H, Baghshahi S, Sedghi A. Impact of functionalized SiC nano-whisker on the flux pinning ability and superconductor features of Bi-2223 ceramics. *Ceram Int* 2021;47:3706–12. <https://doi.org/https://doi.org/10.1016/j.ceramint.2020.09.226>.
55. Kameli P, Salamati H, Abdolhosseini I. AC susceptibility study of Bi_{1.66}Pb_{0.34}Sr₂Ca₂ – xMg_xCu₃O_y (x = 0, 0.2 and 0.4) superconductor systems. *J Alloys Compd* 2008;458:61–5. <https://doi.org/http://dx.doi.org/10.1016/j.jallcom.2007.04.043>.
56. Slimani Y, Almessiere MA, Hannachi E, Mumtaz M, Manikandan A, Baykal A, et al. Improvement of flux pinning ability by tungsten oxide nanoparticles added in YBa₂Cu₃O_y superconductor. *Ceram Int* 2019;45:6828–35. <https://doi.org/10.1016/j.ceramint.2018.12.176>.
57. Guner SB, Zalaoglu Y, Turgay T, Ozyurt O, Ulgen AT, Dogruer M, et al. A detailed research for determination of Bi/Ga partial substitution effect in Bi-2212 superconducting matrix on crucial characteristic features. *J Alloys Compd* 2019;772:388–98. <https://doi.org/10.1016/j.jallcom.2018.09.071>.
58. Choi WJ, Seo YI, Ahmad D, Kwon YS. Thermal activation energy of 3D vortex matter in NaFe₁ – xCo_xAs (x = 0.01, 0.03 and 0.07) single crystals. *Sci Rep* 2017;7:10900. <https://doi.org/10.1038/s41598-017-11371-1>.
59. Palstra TTM, Batlogg B, Schneemeyer LF, Waszczak J V. Thermally Activated Dissipation in Bi_{2.2}Sr₂Ca_{0.8}Cu₂O₈. *Phys Rev Lett* 1988;61:1662–5. <https://doi.org/10.1103/PhysRevLett.61.1662>.
60. Blatter G, Feigel'man M V, Geshkenbein VB, Larkin AI, Vinokur VM. Vortices in high-temperature superconductors. *Rev Mod Phys* 1994;66:1125–388. <https://doi.org/10.1103/RevModPhys.66.1125>.
61. Ahmad D, Choi WJ, Seo YI, Seo S, Lee S, Kwon YS. Thermally activated flux flow in superconducting epitaxial FeSe_{0.6}Te_{0.4} thin film. *Results Phys* 2017;7:16–20. <https://doi.org/https://doi.org/10.1016/j.rinp.2016.11.054>.
62. Lee H-S, Bartkowiak M, Kim JS, Lee H-J. Magnetic-field-induced crossover of vortex-line coupling in SmFeAsO_{0.85} single crystal. *Phys Rev B* 2010;82:104523. <https://doi.org/10.1103/PhysRevB.82.104523>.
63. Zhang YZ, Wen HH, Wang Z. Thermally activated energies of YBa₂Cu₃O₇ and Y_{0.8}Ca_{0.2}Ba₂Cu₃O₇ thin films. *Phys Rev B* 2006;74:144521. <https://doi.org/10.1103/PhysRevB.74.144521>.
64. Zhang YZ, Ren ZA, Zhao ZX. Thermally activated energy and critical magnetic fields of SmFeAsO_{0.9}F_{0.1}. *Supercond Sci Technol* 2009;22:65012. <https://doi.org/10.1088/0953-2048/22/6/065012>.
65. Venkateshwarlu D, Ganesan V, Ohashi Y, Kikkawa S, Yakhmi J V. TAFF and vortex glass state in a niobium oxy-nitride Nb(N_{0.98}O_{0.02}). *Supercond Sci Technol* 2015;28:55009. <https://doi.org/10.1088/0953-2048/28/5/055009>.
66. Fisher MPA. Vortex-glass superconductivity: A possible new phase in bulk high T_c oxides. *Phys Rev Lett* 1989;62:1415–8. <https://doi.org/10.1103/PhysRevLett.62.1415>.

67. Liu SL, Wu GJ, Xu XB, Wu J, Shao HM. Scaling of the vortex–liquid resistivity in high temperature superconductors. *Supercond Sci Technol* 2005;18:1332–6. <https://doi.org/10.1088/0953-2048/18/10/014>.
68. Hannachi E, Slimani Y, Ekicibil A, Manikandan A, Ben Azzouz F. Excess conductivity and AC susceptibility studies of Y-123 superconductor added with TiO₂ nano-wires. *Mater Chem Phys* 2019;235:121721. <https://doi.org/10.1016/j.matchemphys.2019.121721>.
69. Ansari IA. Study of dynamic behaviors for nano Fe-doped MgB₂ superconductor via ac-susceptibility measurements. *Ceram Int* 2019;45:1523–7. <https://doi.org/10.1016/j.ceramint.2018.10.025>.
70. Slimani Y, Almessiere MA, Hannachi E, Manikandan A, Algarni R, Baykal A, et al. Flux pinning properties of YBCO added by WO₃ nanoparticles. *J Alloys Compd* 2019;810:151884. <https://doi.org/10.1016/j.jallcom.2019.151884>.
71. Clem JR. Granular and superconducting-glass properties of the high-temperature superconductors. *Phys C Supercond* 1988;153–155:50–5. [https://doi.org/https://doi.org/10.1016/0921-4534\(88\)90491-1](https://doi.org/https://doi.org/10.1016/0921-4534(88)90491-1).

Figures

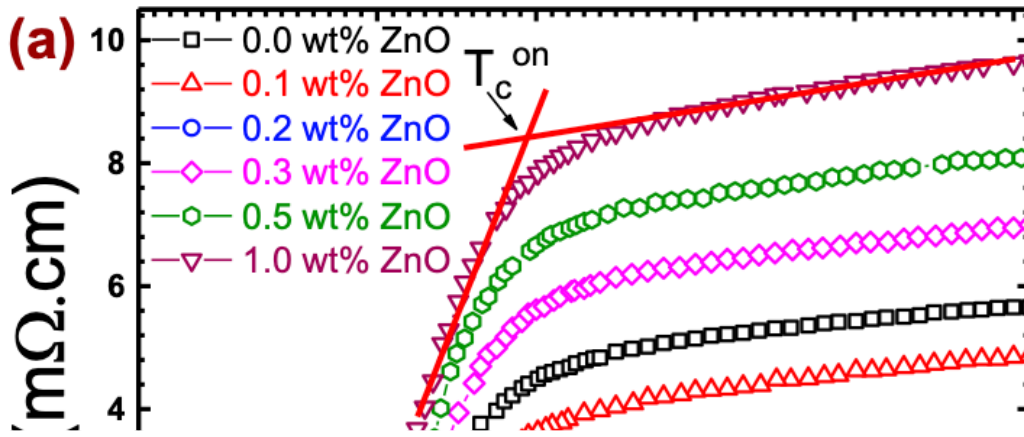


Figure 1

(a) Plots of the temperature dependence of electrical resistivity $\rho(T)$ and (b) it's corresponding derivative $d\rho/dT$ for the different (Bi, Pb)-2223 / (ZnO NPs) $_x$ composites.

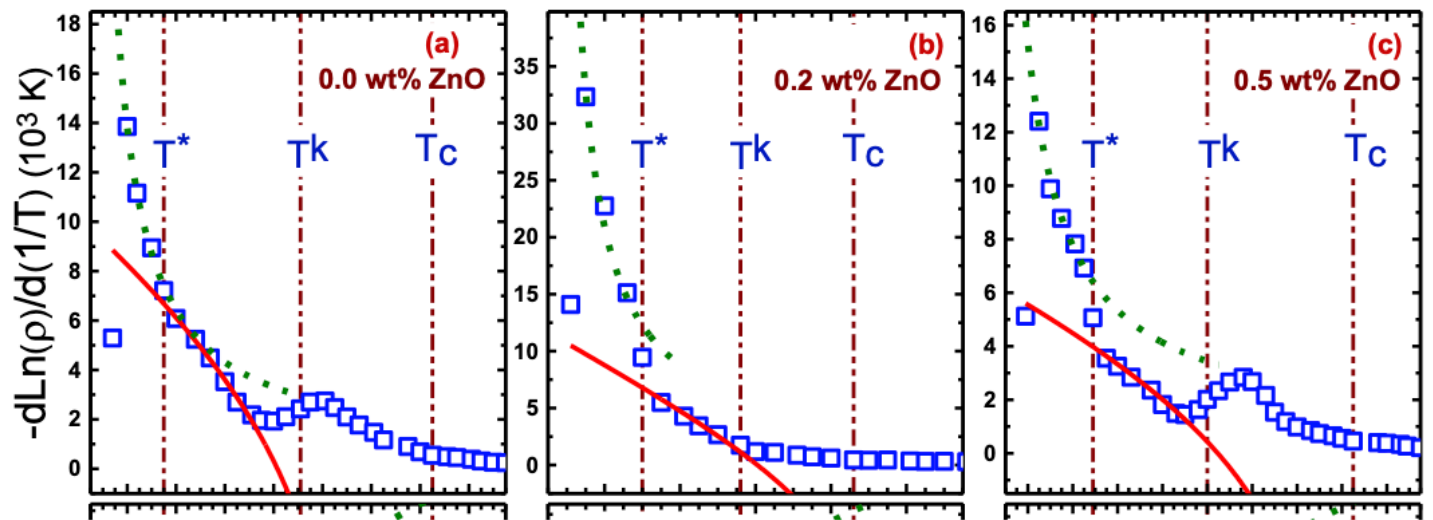


Figure 2

See image above for figure legend.

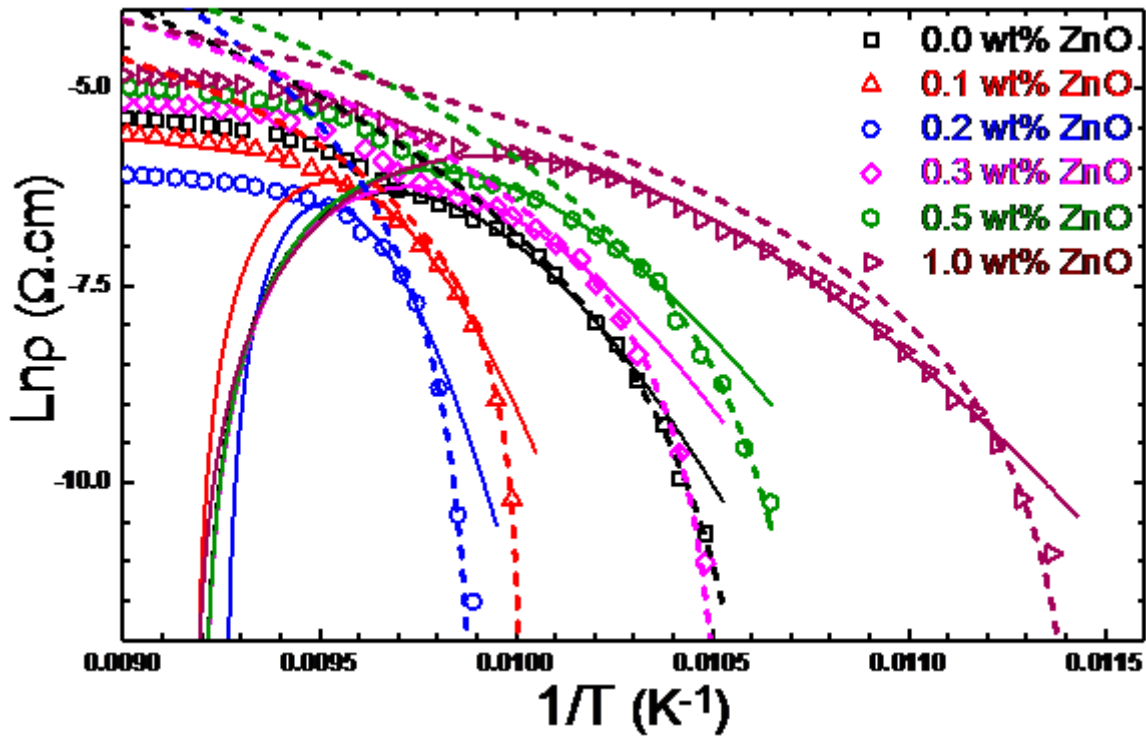


Figure 3

The $\text{Ln } \rho$ vs. $1/T$ curves for different (Bi, Pb)-2223 / (ZnO NPs) $_x$ composites. The solid lines are the fits according to Eq. (5) and the dashed lines are the fits according to Eq. (9).

Figure 4

Variations of the zero-temperature activation energy U_0 , with respect to the ZnO NPs contents.

Figure 5

See image above for figure legend.

Figure 6

Temperature dependence of **(a)** the real part of AC susceptibility, χ' , **(b)** and its derivative, $d\chi'/dT$, for different (Bi, Pb)-2223 / (ZnO NPs) $_x$ composites, measured at magnetic field amplitude of 250 A/m and frequency of 300 Hz. **(c)** Variations of the inter-granular coupling temperature, T_{CJ} , and Josephson coupling energy, E_j , with respect to the ZnO NPs contents.

Figure 7

V-J curve for different (Bi, Pb)-2223/(ZnO NPs)_x composites at 77 K.